Geophysical Journal International

Geophys. J. Int. (2017) **210,** 284–290
Advance Access publication 2017 April 26
GJI Rock and mineral physics, rheology

doi: 10.1093/gji/ggx160

Network topology of olivine–basalt partial melts

Philip Skemer,[1] Molly M. Chaney,[2] Adrienne L. Emmerich,[1] Kevin J. Miller[3] and Wen-lu Zhu[4]

[1] *Washington University in Saint Louis, Saint Louis, MO* 63130*, USA. E-mail: pskemer@wustl.edu*
[2] *Princeton University, Princeton, NJ* 08540*, USA*
[3] *Stanford University, Palo Alto, CA* 94305*, USA*
[4] *University of Maryland, College Park, MD* 20742*, USA*

Accepted 2017 April 21. Received 2017 April 19; in original form 2017 March 1

SUMMARY

The microstructural relationship between melt and solid grains in partially molten rocks influences many physical properties, including permeability, rheology, electrical conductivity and seismic wave speeds. In this study, the connectivity of melt networks in the olivine–basalt system is explored using a systematic survey of 3-D X-ray microtomographic data. Experimentally synthesized samples with 2 and 5 vol.% melt are analysed as a series of melt tubules intersecting at nodes. Each node is characterized by a coordination number (CN), which is the number of melt tubules that intersect at that location. Statistically representative volumes are described by coordination number distributions (CND). Polyhedral grains can be packed in many configurations yielding different CNDs, however widely accepted theory predicts that systems with small dihedral angles, such as olivine–basalt, should exhibit a predominant CN of four. In this study, melt objects are identified with CN = 2–8, however more than 50 per cent are CN = 4, providing experimental verification of this theoretical prediction. A conceptual model that considers the role of heterogeneity in local grain size and melt fraction is proposed to explain the formation of nodes with CN $\neq$ 4. Correctly identifying the melt network topology is essential to understanding the relationship between permeability and porosity, and hence the transport properties of partial molten mantle rocks.

Key words: Microstructure; Permeability and porosity; Mantle processes.

1 INTRODUCTION

Beneath mid-ocean ridges, adiabatic decompression produces partial melt in ascending mantle peridotite. The buoyant melt formed by this process rises through the mantle, is focused towards the ridge axis, and forms new oceanic crust. The chemical and physical properties of the upper mantle and lower crust are strongly influenced by the permeability and melt distribution of the partially molten rocks (McKenzie 1984; Spiegelman & McKenzie 1987; Kelemen *et al.* 1997).

There exist contradicting views on melt distribution beneath mid-ocean ridges. The uranium decay series disequilibria in mid-ocean ridge basalts implies a well-connected, permeable mantle for rapid melt segregation at melt fractions as low as 0.01 (e.g. Johnson *et al.* 1990; Lundstrom *et al.* 1995; Salters & Longhi 1999). In contrast, geophysical surveys detect a broad low-velocity region (e.g. The Melt Seismic Team 1998; Evans *et al*. 1999), which are interpreted as evidence for high melt fractions beneath the ridge. A recent magnetotelluric study suggests that local melt fractions may be as high as 0.10 (Key *et al.* 2013).

Permeability (Riley & Kohlstedt 1991; Wark & Watson 1998; Renner *et al.* 2003; Bernabé *et al.* 2010) and electrical conductivity (Waff 1974; Yoshino *et al.* 2010) are sensitive to the volume, composition and spatial distribution of melts. Understanding the 3-D melt microstructure in idealized systems, such as olivine plus basalt melt, is critical for interpreting a wide range of experimental and geological observations, and for creating models of geochemical and geophysical processes. To reconcile the discrepancies of current results, the first step is to obtain more accurate descriptions of the relationship between permeability (or electrical conductivity) and the melt distribution.

In partially molten systems, minimization of interfacial energy predicts various types of melt networks, which range from fully connected melt channels to isolated melt pockets (e.g. Smith 1964; Kingery *et al.* 1976). The connectivity of the melt depends on the dihedral or wetting angle of the liquid–solid interface, the volume of melt present and the grain shape. Crystalline materials can be packed in a variety of space-filling configurations and different grain shapes have been used to model partially molten rocks. Bulau *et al*. (1979) modeled grains as truncated octahedra, a space-filling tetrakaidecahedron with 14 faces. With this geometry, melt is predicted to reside along edges, where three grains meet, and in corners, where four grains meet. Many subsequent numerical studies have adopted this geometry to calculate permeability

© The Authors 2017. Published by Oxford University Press on behalf of The Royal Astronomical Society.

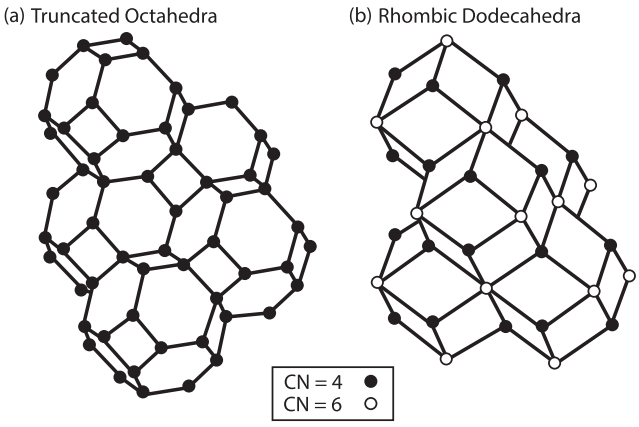

Figure 1. Two idealized models for polycrystalline edge connectivity based on standard tessellated polyhedra (e.g. Cromwell 1999). (a) Truncated octahedra, for which every grain corner is associated with four grain edges, yielding a coordination number of CN = 4. (b) Rhombic dodecahedra for which each grain corner is formed by the intersection of either four or six grains. Half of the corners are CN = 4 and half are CN = 6.

(von Bargen & Waff 1986; Zhu & Hirth 2003). Park & Yoon (1985) argue that rhombic dodecahedral grains with 12 faces are suitable for simulating polycrystals, and grains with this shape have been used to model elastic wave velocity of the partially molten rocks (e.g. Takei 2002). Different space-filling polyhedral grain shapes produce different numbers of connecting melt tubules, which we define as the coordination number (CN). For example, if grains are packed in a truncated octahedral configuration, four grains meet at every corner (Bulau *et al.* 1979, Fig. 1a), and CN = 4. If grains are packed in a rhombic dodecahedral configuration, either four or six grains meet at corners (*cf.* Cromwell 1999, Fig. 1b), thus CN = 4 or 6. The CN is a direct measure of melt connectivity, which exerts an important control on the permeability of partially molten rocks. It has been shown that in general, for a given porosity, networks with higher CN are more permeable (e.g. Bernabé *et al.* 2010). Hence, accurate determination of the CN is needed to provide better constraints on models of grain shape and permeability, and to interpret experimental results.

The geometry of melt networks in experimental studies has been described largely using 2-D imaging coupled with theory to extrapolate into the third dimension (e.g. Jurewicz & Jurewicz 1986). True 3-D microstructure has been described only recently using either serial sectioning methods (Wark *et al.* 2003; Garapić *et al.* 2013) or synchrotron-based X-ray microtomography (Watson & Roberts 2011; Zhu *et al.* 2011). Microtomographic imaging provides high-resolution imagery of the 3-D melt distribution over a relatively large volume. This method is therefore ideal for quantifying melt connectivity, although the resolution does not permit observation of thin (10–100 nm) melt films that may be seen with electron microscopy (Garapić *et al.* 2013). In Zhu *et al.* (2011), the connectivity of melt was evaluated using a skeletonization algorithm to reduce the melt network to a series of tubules and nodes. The CN of the nodes, which describes the number of melt channels connected to each melt corner, was determined using this reduced data set. The experimental samples in the Zhu *et al.* (2011) study exhibit a broad range of CNs, from CN = 1 to 9, and several samples are characterized by coordination number distributions (CND) with modes of less than four. Although Zhu *et al.* (2011) document a substantial population of nodes with CN > 4, the numerical approach could not distinguish between different grain configurations, such as those as illustrated in Fig. 1. To further investigate the microstructure and connectivity of these melt networks, we have revisited the 3-D tomographic data using a direct survey approach to characterize within resolution limits the shapes of melt objects and to measure the frequency distribution of CN in olivine–basalt samples with 2–5 vol.% melt.

2 METHODS

Samples investigated in this study were synthesized from mixtures of San Carlos olivine and high-alumina basalt in a solid medium piston-cylinder apparatus. Quenched experimental run products were analysed using synchrotron-based X-ray microtomography at the Advanced Photon Source at Argonne National Laboratory (see Zhu *et al.* 2011 and Miller *et al.* 2014 for complete details of sample synthesis and microtomographic data collection). Two samples are examined in this study: scoba-9 (2 vol.% melt), which was annealed for 336 hr and scoba-12 (5 vol.% melt), which was annealed for 168 hr (Table 1). The average grain size of both samples is ∼40 μm, and the samples are inferred to be in microstructural equilibrium (Miller *et al.* 2014).

Data were processed and reduced to binary form so that solid olivine is distinguishable from basalt glass. Subsets of these data were created, corresponding to cubes with an edge length of 500 pixels (350 μm) for scoba-9 (2 per cent melt) and 200 pixels (140 μm) for scoba-12 (5 per cent melt). Data were converted to isosurfaces, which delineate the boundary between solid and melt. These 3-D microstructural data sets are identical to those described in Zhu *et al.* (2011) and Miller *et al.* (2014); no additional smoothing or filtering was imposed. Data were imported into ArcScene software for 3-D visualization and a grid system was superimposed on the data to facilitate a spatially systematic survey of the melt geometry (Fig. 2). For some analyses, data were projected into the Fossett 3-D visualization cave at Washington University in Saint Louis (Fig. 3).

Data are interpreted as a series of melt tubules, assumed to form at grain edges, connected at nodes, which are assumed to form within pores at grain corners. Nodes are characterized by the number of connecting tubules, which we define as the CN. The size of the nodes, or pores, is determined by measuring their length in three orthogonal directions and calculating the diameter of an equivalent sphere. Melt objects are identified visually using the following criteria: (1) nodes are identified as the junction where two or more distinct tubules meet. The terminus of a single tubule is not interpreted to be a unique node unless an obvious volume of melt is present, with a diameter significantly larger than the diameter of the associated tubule. (2) Tubules are classified as such if their

Table 1. Number of nodes and node density for samples investigated in this study.

Sample	Melt fraction	Number of nodes (this study)	Density of nodes [m^{-3}] (this study)	Number of nodes (Miller *et al.* 2014)	Density of nodes [m^{-3}] (Miller *et al.* 2014)
scoba-09	0.02	206	4.8×10^{12}	635	1.5×10^{13}
scoba-12	0.05	175	6.4×10^{13}	3407	8.0×10^{13}

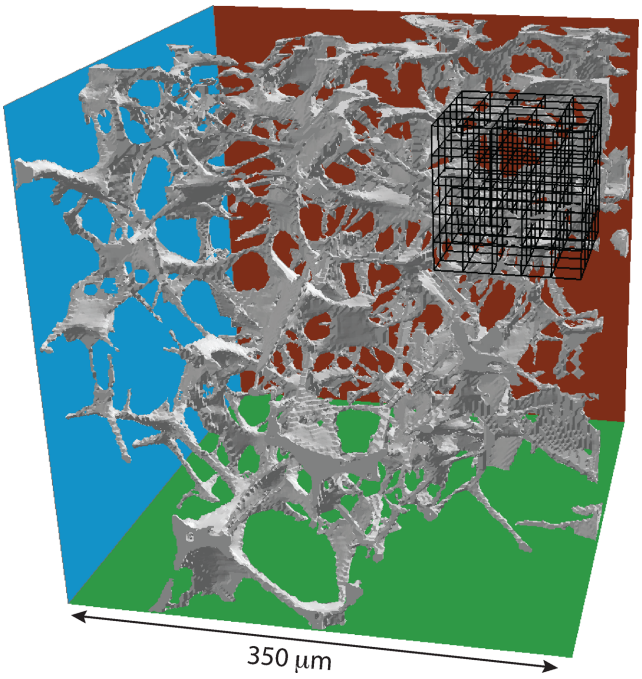

Figure 2. Melt network for sample scoba-12 (5 per cent melt) with a superimposed grid system used for systematic surveying. Grey objects represent melt and open spaces are the olivine matrix.

minimum length is greater than or equal to the diameter of the associated node. (3) Nodes with tubules that appear to be truncated by the edge of the data space are not included in the analysis unless their CN can be confidently inferred. Typically, this requires the node centre to be at least 10 μm from the edge of the data space. (4) Clusters of melt or nodes with large CN (CN $>$ 4) are split into their component nodes when clear distinctions can be made. For example, a cluster that appears to have six tubules could be classified as two discrete nodes with four tubules each if the two nodes are connected by a tubule that is long enough to be counted according to criterion (2).

3 RESULTS

A variety of melt objects were identified using this direct survey approach. The CN of these objects range from CN = 2 to 8. Examples of nodes with different CN are shown in Fig. 4.

The connectivity of the melt networks is quantified using CND, which show the normalized frequency of melt objects with a given number of associated melt tubules (Fig. 5). For sample, scoba-9 (2 vol.% melt), 206 melt objects were identified over a volume of 4.3×10^7 μm^3 (a cube with edge length 350 μm), corresponding to a melt object density of 4.8×10^{12} m^{-3} (Table 1). Within this volume, there are ∼100 grains (Miller *et al.* 2014), and so an average of two melt objects per grain were identified. The CND has a mode of four, with 69.4 per cent of nodes populating this category (Fig. 5a). Nodes with CN = 3 are the next most abundant, making up 17.5 per cent of all observed nodes. 12.6 per cent of nodes have CN of 5 or 6. Only one node was identified with a CN = 2 (<1 per cent of all nodes). No nodes with a CN $\geq$ 7 were observed.

For sample scoba-12 (5 per cent melt), data collection was performed three times by two different authors to test for reproducibility and analytical bias. In total, 175 ± 9 melt objects were identified over a volume of 2.7×10^6 μm^3 (a cube with edge length 140 μm), giving this sample an average melt object density of 6.4×10^{13} m^{-3} (Table 1). Within this volume, there are ∼30 grains (Miller *et al.* 2014), and thus an average of approximately six melt objects per

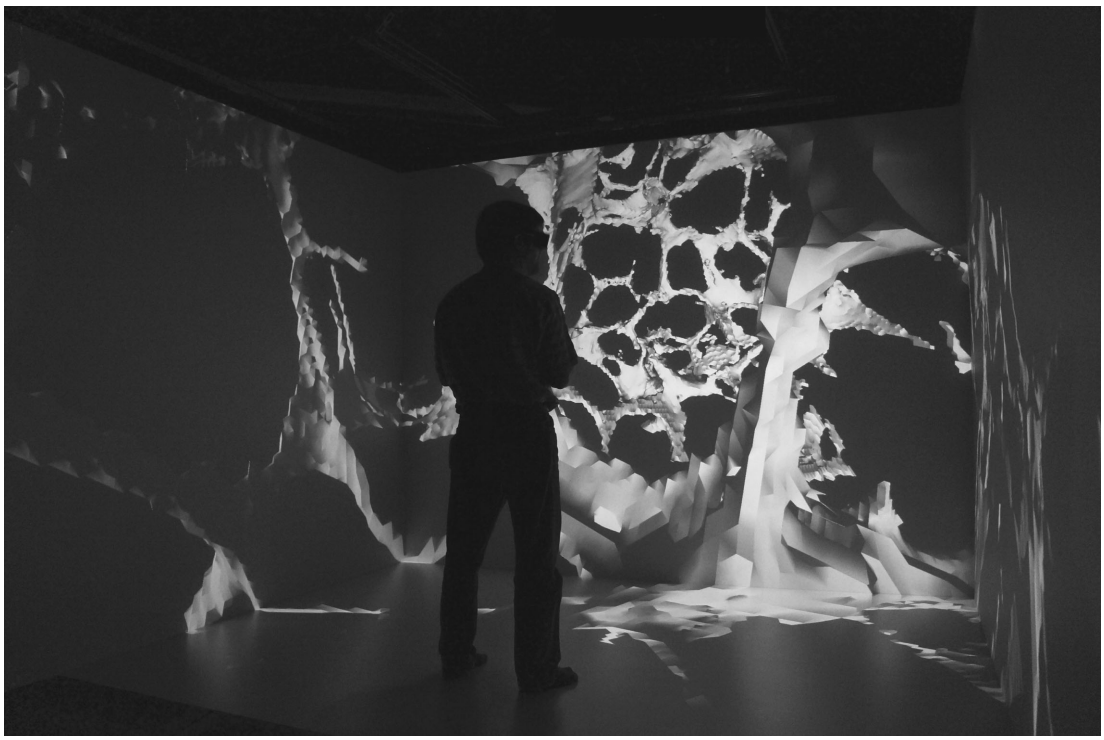

Figure 3. Data projected in the 3-D visualization cave in the Fossett Laboratory for Virtual Planetary Exploration at Washington University in Saint Louis. The visualization cave projects data onto three walls and the floor. Users, wearing 3-D glasses, are able to 'fly' into the sample and readily view objects from several orientations that might be obscured by other microstructural features.

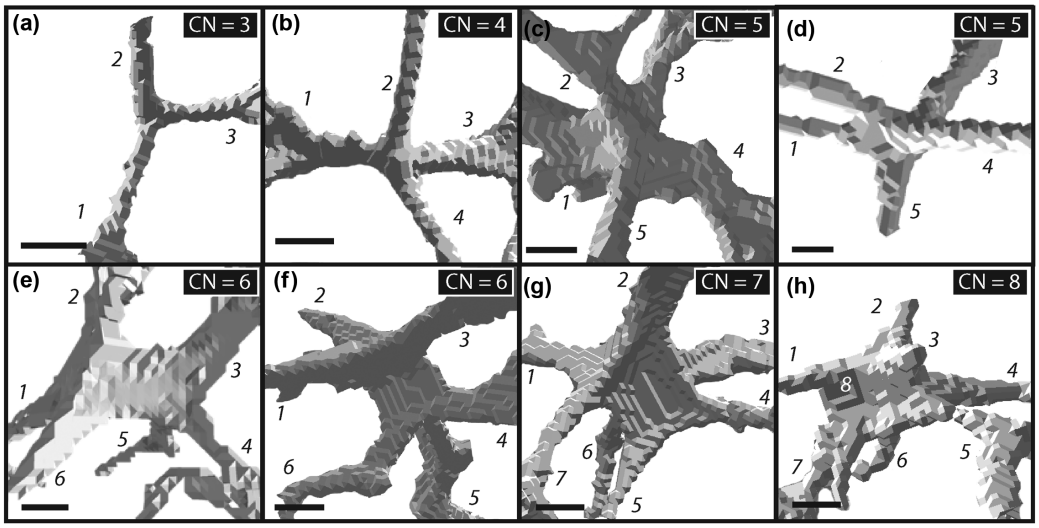

Figure 4. Examples of melt objects with coordination numbers (CN) ranging from 3 to 8. The tubules associated with each node are numbered. Scale bars are 10 μm.

grain. The CND for scoba-12 was created using the average, with 1σ error shown, of the three separate analyses (Fig. 5b). This sample was also found to have a mode CN of four; 50.9 per cent of nodes had CN = 4. CN = 3 is the second most abundant category, representing 20.1 per cent of nodes. Only two melt objects, <1 per cent of the total, have a CN = 2. Nodes with CN ≥ 5 make up 27.6 per cent of the objects identified.

4 DISCUSSION

The geometry of melt in isotropic materials can be predicted from theory if the dihedral angle of the system is known. von Bargen & Waff (1986) demonstrate that theoretical systems with a dihedral angle smaller than 60° will always exhibit a completely interconnected melt network at melt fractions of 0.005 or lower. For systems with dihedral angles greater than 60°, melt will not form an interconnected network unless the system is above a critical melt fraction. A number of experimental studies have characterized the distribution of dihedral angles in the olivine–basalt system. Waff & Bulau (1979), investigating samples equilibrated at high temperature and pressure, observe a median dihedral angle of 47°, below the critical threshold for interconnectivity at low melt fractions. Further microscopic study corroborated this observation, and also confirmed the absence of melt films along boundaries between two olivine grains (Vaughan & Kohlstedt 1982), although this latter conclusion has been debated (Garapić *et al.* 2013). Based on theory and experiments, it is generally assumed that the melt in the olivine–basalt system will form an interconnected network characterized by nodes with a predominant CN of four (Fig. 5a).

In an ideal system of isotropic surface energy and uniform grain size, melt topology at textural equilibrium is characterized by a constant mean curvature, and a correspondingly constant dihedral angle (Smith 1964; von Bargen & Waff 1986). However, in the olivine–basalt system, dihedral angle may not be constant, which could lead to more complex melt geometries. For example, anisotropic surface energy (Waff & Bulau 1979; Cooper & Kohlstedt 1982; Vaughan & Kohlstedt 1982; Laporte & Watson 1995), and the presence of faceted grains (Cmíral *et al.* 1998; Price *et al.* 2006; Yoshino *et al.* 2006), may introduce variation in the dihedral angle as a function of crystallographic orientation and texture. Grain-scale heterogeneities, such as non-uniform grain size and grain shapes that do not conform to the idealized foam-textured tetrakaidecahedra (e.g. Kingery *et al.* 1976) may modify melt geometry in a way that is not captured by isotropic theory (Bulau *et al.* 1979; Wark & Watson 2000). Finally, while not strictly relevant to this study, theory and experiments suggest that under non-static conditions melt will segregate through dynamic pressure gradients into bands of relatively high and low melt concentration, modifying the distribution of melts in partially molten rocks (Holtzman *et al.* 2003; Kohlstedt & Holtzman 2009).

Previous efforts by Zhu *et al.* (2011) to quantify melt connectivity in three dimensions used a skeletonization algorithm to reduce melt networks to a series of nodes connected by tubules, from which CNDs are readily calculated. This method is efficient, and capable of processing data from large sample volumes. However, there are limitations to this algorithm that impose artefacts on the resulting data. For example, any terminus in the melt network is identified as a node, with a CN equal to one. Therefore, the number of nodes with CN = 1 is likely overestimated. Furthermore, the algorithm was purposefully configured to exclude nodes with CN = 2, as these do not modify the sample's permeability. Hence, the CNDs from Zhu *et al.* (2011) do not contain any data with CN = 2. Larger clusters of melt, with closely spaced nodes or unusually shaped tubules are also difficult for the algorithm to parse, which leads to a preponderance of nodes with CN > 4. The method used in this study, while relatively labor intensive, provides a more accurate view of the coordination of the melt networks. Objects that occur at the terminus of a melt tubule are readily identified as places where the melt pinches out, or becomes narrower than the spatial resolution of the microtomography technique (~0.7 μm). Nodes with large CNs can be evaluated in the context of the local microstructure to determine whether they are singular objects, or closely spaced clusters of smaller objects. In doing so, we gain a richer picture of the grain-scale organization of crystalline and molten material (Figs 2 and 4).

Considerable differences are observed between the CNDs for scoba-9 (2 per cent melt) determined by our survey and by Zhu *et al.* (2011, Fig. 5a). First, our microstructural analysis indicates that the large number of objects with CN = 1 (49.8 per cent) identified by the skeletonization algorithm are places where melt tubules

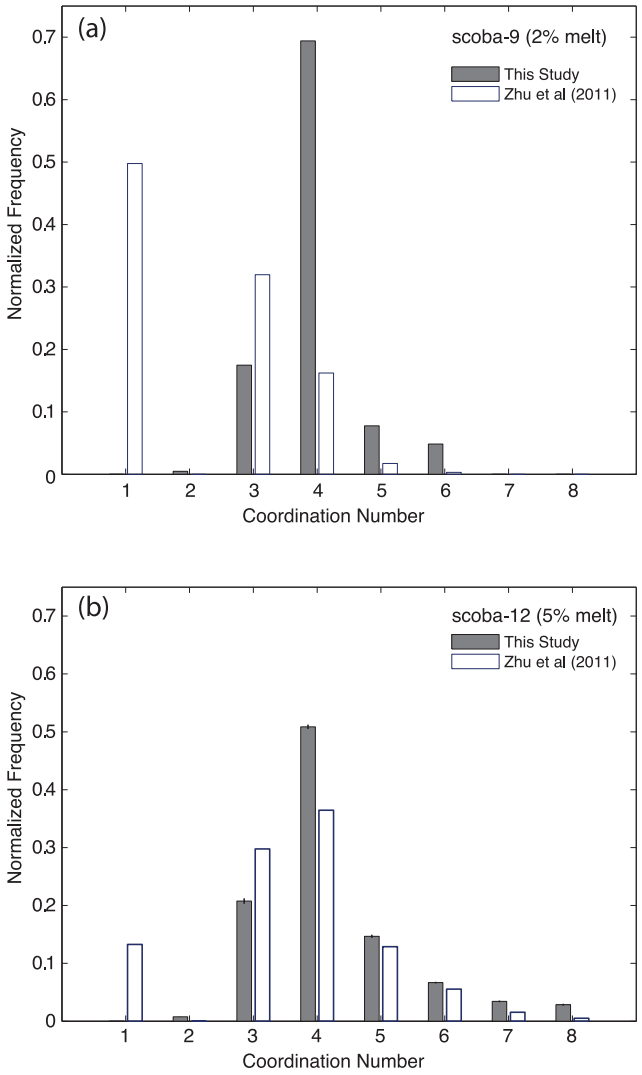

Figure 5. Coordination number distributions (CND) for samples (a) scoba-9 (2 per cent melt) and (b) scoba-12 (5 per cent melt, bottom). Grey bars are the CNDs for this study, determined using a direct survey approach. White bars are the CNDs reported by Zhu *et al*. (2011), determined using an automatic computer algorithm. Short black lines on the scoba-12 CND are 1σ errors from the mean of three independent analyses. While there is some variation in the interpretation of individual objects, the three analyses of scoba-12 and hence the distributions are quite similar.

pinch out or are truncated by the edge of the data space, not true nodes. Second, the survey data demonstrate that nodes with CN = 4 clearly dominate the melt network, in contrast to the relatively small fraction of nodes (16.2 per cent) with CN = 4 identified by Zhu *et al*. (2011). These observations also confirm that the abundance of nodes with CN = 3 detected by the algorithm is indeed an artefact of resolution limits, as suggested by Zhu *et al*. (2011). The density of melt objects detected by the algorithm is three times greater than the density of objects detected by the survey approach (Table 1), which is interpreted to be a result of misidentified nodes with CN = 1.

The CNDs for scoba-12 (5 per cent melt) determined by this study and by Zhu *et al*. (2011) are more comparable (Fig. 5b). Both methods find the mode of the CND to be equal to four, although this study identifies a greater abundance of nodes with CN = 4 and none with CN = 1, leading to a narrower distribution of CNs. For scoba-12, the density of objects identified by the two methods is similar, with the algorithm identifying approximately 25 per cent more objects than the survey approach (Table 1).

In this study, CNDs determined for olivine samples with 2–5 per cent basaltic melt exhibit a mode CN of four (Fig. 5), consistent with theoretical predictions of Bulau *et al.* (1979). Moreover, the distributions are narrow, and nodes with CN = 4 represent greater than 50 per cent of the objects identified. In both samples, the second most abundant nodes are those with CN = 3 (Fig. 3). We interpret these objects as nodes for which one of the four associated edges does not exhibit evidence of melting. The data do not allow us to distinguish between grain edges that contain no melt, and grain edges for which the local melt fraction was below detectable limit of the current microtomography technique.

As discussed earlier, the olivine–basalt system is not strictly isotropic and homogeneous, which could lead to grain-scale variation in melt fraction. If locally varying melt fraction is a feature of the olivine–basalt system, edges with lower than average melt fraction must be compensated for elsewhere by sites with higher local melt fractions. Indeed, locally elevated melt fractions seem to be a characteristic of melt objects with larger CNs. Figs 4(c)–(h) show several examples of melt objects with CN > 4. However, detailed examination of nodes with CN > 4 reveals that the majority of these objects are actually formed by joining closely spaced melt corners into a large pocket of melt. Objects with CN = 6 are particularly instructive (Figs 4e and f). Based on the shape and spacing of the melt tubules and nodes, we infer that CN = 6 nodes are formed by two adjoining CN = 4 nodes connected by a short and wide melt tubule. The short length of the connecting tubule is a consequence of the comparatively small size of the three adjacent grains. The width and volume of the connecting tubule may be related to locally elevated melt concentration. The three smaller grains that surround the connecting melt tubule, plus the two larger grains that form the opposite ends of the CN = 6 node, yield a melt object constructed of the interfaces between five grains. No true CN = 6 nodes, in which six melt tubules and six grains meet at a single grain corner, were observed in this survey. Based on these microstructural observations, we propose that most of CN > 4 nodes are formed by linking two or more closely spaced CN = 4 nodes (Fig. 4) and are not a result of true six-grain junctions (Fig. 1b). Therefore, we conclude that the olivine packing is best modeled by truncated octahedral grains; grains packed in a rhombic dodecahedral configuration are inconsistent with our results.

The coalescence of CN = 4 nodes into melt objects with CN > 4 may be due to (1) dissimilar grain size between adjacent grains, leading to short connecting tubules and/or (2) a large local melt fraction that causes melt to 'overflow' into the grain boundaries, as is expected for larger melt fractions (von Bargen & Waff 1986). As illustrated in Figs 4(e) and (f), and 6(b), connecting two standard CN = 4 nodes forms an object with CN = 6. Connecting three standard nodes in a line or four nodes in a closed loop, produces an object with CN = 8 (Fig. 6c). Objects with odd CNs (CN = 5 or 7) may be generated in a similar way through combinations of nodes with CN = 3 and 4. With melt fractions between 2 and 5 per cent, we consider it unlikely that more than four corners should become connected in this manner, and indeed no objects were identified with CN > 8. Although not analysed in this study, Zhu *et al*. (2011) found that in a sample with 20 per cent melt, some grain boundaries are wet and objects with CN = 9 are found. Note that there are more objects with CN > 4 in higher melt fraction sample scoba-12 (5 per cent melt) than those in scoba-9 (2 per cent melt), and that objects with CN = 8 are observed in scoba-12 only (Fig. 5), which

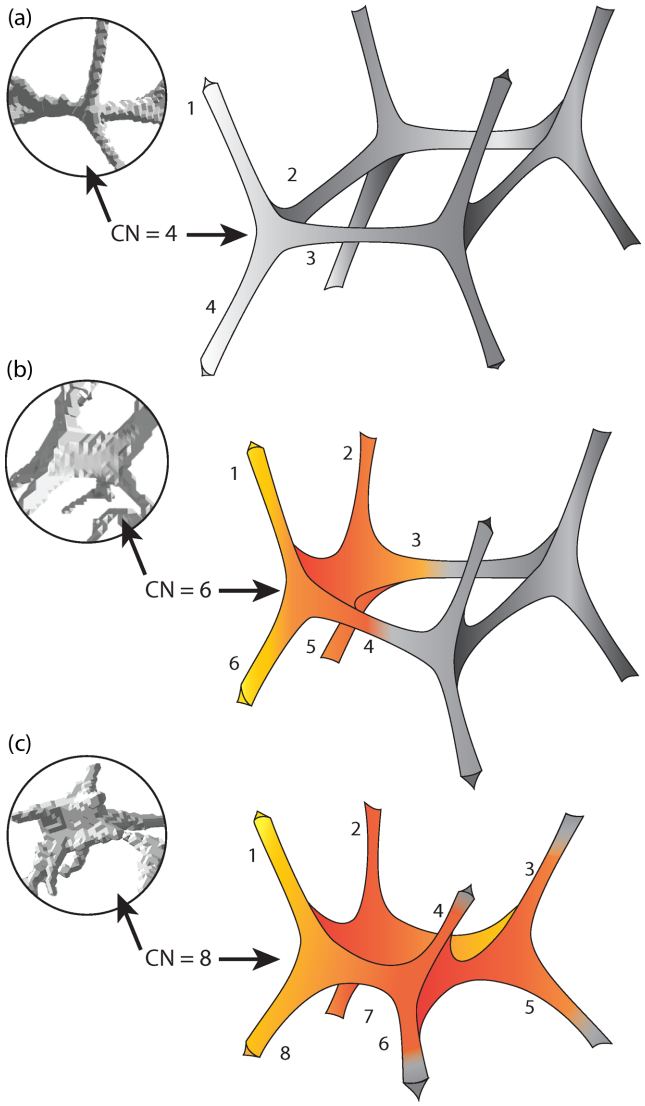

Figure 6. Schematic diagrams of melt networks for (a) CN = 4; (b) CN = 6 and (c) CN = 8. Inset figures show examples of nodes with these coordination numbers (see also Fig. 4). Nodes with CN = 4 are the most abundant melt objects in this study, and networks composed of CN = 4 are predicted to represent the equilibrium melt texture in the olivine–basalt system. Nodes with coordination numbers greater than four are interpreted to be formed by the coalescence of two or more standard nodes. The connection of these nodes may be due in part to local variation in the grain size, which shortens the lengths of some tubules, as well as locally elevated melt fractions.

is consistent with the 'melt overflow' conceptual model illustrated in Fig. 6.

In general, permeability of a porous rock depends on both pore-size distribution and pore connectivity, and the latter can be characterized by the average CN. Using network model simulations, Bernabé *et al.* (2010) derived 'universal' power-law relationships between permeability k and the average CN z of the network:

$$k \sim (z - z_c)^{\beta} \quad (1)$$

where $z_c = 1.5$ for 3-D pore networks. Parameter β is a non-dimensional constant that depends on the normalized standard deviation of the tubule diameter σ_r (Bernabé *et al.* 2011):

$$\beta = 1.2343 + 0.93462\sigma_r + 1.4755{\sigma_r}^2 \quad (2)$$

$$\sigma_r = \sigma / \langle r \rangle \quad (3)$$

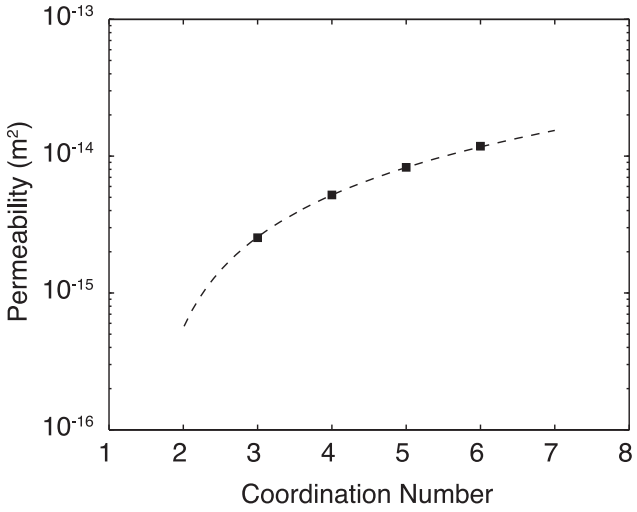

Figure 7. Model from Bernabé *et al.* (2010) showing how permeability depends on coordination number for a given melt fraction and tubule size distribution. For sample scoba-12, an experimentally generated sample with a homogeneous microstructure and narrow grain size distribution, the difference in permeability between a network with CN = 4 (representing truncated octahedral grains) and CN = 5 (representing rhombic dodecahedral grains) is approximately 60 per cent. Samples with more heterogeneous microstructures will exhibit even greater variation in permeability as a function of coordination number.

where σ is the standard deviation of the tubule diameter distribution and $\langle r \rangle$ is the average tubule diameter. For partially molten samples, the throat size of the melt tube is proportional to the grain size (i.e. von Bargen & Waff 1986). Therefore, parameter β can be obtained from the grain size distribution of scoba-12, which is lognormal (Miller *et al.* 2014).

A histogram of grain size from sample scoba-12 is provided by Miller *et al.* (2014); the normalized standard deviation for a lognormal distribution is 0.125, which yields $\beta = 1.37$. In Fig. 7, we model permeability as a function of CN. From the 3-D microtomography data, Miller *et al.* (2014) calculated that the permeability of scoba-12 is 5.2×10^{-15} m^2, which we use to anchor the calculation at $z = 4$. Assuming constant porosity and pore-size distribution, a network comprised of nodes with CN = 4 and 6 would yield an average CN $z = 5$, and would be ~60 per cent more permeable. This represents a conservative lower limit, as scoba-12 is synthesized experimentally and likely more homogeneous (therefore with permeability less sensitive to CN) than heterogeneous natural samples with comparable porosity. The sensitivity of permeability to CN is an important factor that must be considered when constructing numerical models of flow in porous media.

5 CONCLUSIONS

This study presents the first visual, 3-D survey of melt network coordination in the olivine–basalt system. Our survey approach represents a marked improvement over previous approaches by deciphering the CN and providing a more accurate picture of melt network microstructure at the level of individual melt pockets and tubules. Over a range of melt fractions (2–5 vol.%), melt forms an interconnected network, with tubules along grain edges meeting at melt nodes located at grain corners. A range of connectivity is observed, with CNs ranging from CN = 2 to 8. Conceptually, this variability in the melt network microstructure reflects the complexities introduced by anisotropic surface energy and variations in grain

size, leading to local variation in melt content. Our data indicate that most of CN > 4 nodes are formed by the coalescence of two or more closely spaced melt nodes. Although the melt microstructures are complex, the predominant CN is four. Therefore, it is concluded the grain packing in the olivine–basalt system is better approximated by truncated octahedra (Bulau *et al.* 1979) than rhombic dodecahedra (Park & Yoon 1985). This result confirms experimentally the theoretical prediction of melt connectivity proposed by Bulau *et al*. (1979).

ACKNOWLEDGEMENTS

The authors thank Bill Winston and Washington University Data and GIS Services for assistance with ArcScene and projection of the data in the Fossett Lab for Virtual Planetary Exploration. Ian Jackson and one anonymous reviewer are thanked for their constructive comments. This work is partially supported by the National Science Foundation EAR-1352306 (to PS) and EAR-1250338 (to WZ), and a grant from the Washington University Office of Undergraduate Research (to MMC). Microtomographic data for this paper are available upon request.

REFERENCES

Bernabé, Y., Li, M. & Maineult, A., 2010. Permeability and pore connectivity: a new model based on network simulations, *J. geophys. Res.,* **115,** B10203, doi:10.1029/2010JB007444.

Bernabé, Y., Zamora, M., Li, M., Maineult, A. & Tang, Y., 2011. Pore connectivity, permeability, and electrical formation factor: a new model and comparison to experimental data, *J. geophys. Res.,* **116,** B11204, doi:10.1029/2011JB008543.

Bulau, J.R., Waff, H.S. & Tyburczy, J.A., 1979. Mechanical and thermodynamic constraints on fluid distribution in partial melts, *J. geophys. Res.,* **84,** 6102–6108.

Cmíral, M., Gerald, J.D.F., Faul, U.H. & Green, D.H., 1998. A close look at dihedral angles and melt geometry in olivine-basalt aggregates: a TEM study, *Contrib. Mineral. Petrol.,* **130,** 336–345.

Cooper, R.F. & Kohlstedt, D.L., 1982. Interfacial energies in the olivine-basalt system, in *High Pressure Research in Geophysics,* pp. 217–228, eds Akimoto, S. & Manghnani, M. H., Center for Academic Publications Japan, Tokyo, Japan.

Cromwell, P.R., 1999. *Polyhedra,* Cambridge Univ. Press.

Evans, R.L. *et al.*, 1999. Asymmetric electrical structure in the mantle beneath the East Pacific Rise at 17°S, *Science,* **286**(5440), 752–756.

Garapić, G., Faul, U. & Brisson, E., 2013. High-resolution imaging of the melt distribution in partially molten upper mantle rocks: evidence for wetted two-grain boundaries, *Geochem. Geophys. Geosyst.,* **14,** 556–566.

Holtzman, B., Groebner, N., Zimmerman, M., Ginsberg, S. & Kohlstedt, D., 2003. Stress-driven melt segregation in partially molten rocks, *Geochem. Geophys. Geosyst.,* **4**(5), 8607, doi:10.1029/2001GC000258.

Johnson, K., Dick, H.J. & Shimizu, N., 1990. Melting in the oceanic upper mantle: an ion microprobe study of diopsides in abyssal peridotites, *J. geophys. Res.,* **95,** 2661–2678.

Jurewicz, S.R. & Jurewicz, A.J., 1986. Distribution of apparent angles on random sections with emphasis on dihedral angle measurements, *J. geophys. Res.,* **91,** 9277–9282.

Kelemen, P.B., Hirth, G., Shimizu, N., Spiegelman, M. & Dick, H.J.B., 1997. A review of melt migration processes in the adiabatically upwelling mantle beneath oceanic spreading ridges, *Phil. Trans. R. Soc. A—Math. Phys. Eng. Sci.,* **355,** 283–318.

Key, K., Constable, S., Liu, L. & Pommier, A., 2013. Electrical image of passive mantle upwelling beneath the northern East Pacific Rise, *Nature,* **495,** 499–502.

Kingery, W., Bowen, H. & Uhlmann, D., 1976. *Introduction to Ceramics,* John Wiley and Sons.

Kohlstedt, D.L. & Holtzman, B.K., 2009. Shearing melt out of the Earth: an experimentalist's perspective on the influence of deformation on melt extraction, *Annu. Rev. Earth planet. Sci.,* **37,** 561–593.

Laporte, D. & Watson, E.B., 1995. Experimental and theoretical constraints on melt distribution in crustal sources: the effect of crystalline anisotropy on melt interconnectivity, *Chem. Geol.,* **124,** 161–184.

Lundstrom, C., Gill, J., Williams, Q. & Perfit, M., 1995. Mantle melting and basalt extraction by equilibrium porous flow, *Science,* **270,** 1958–1961.

McKenzie, D., 1984. The generation and compaction of partially molten rock, *J. Petrol.,* **25,** 713–765.

Miller, K.J., Zhu, W.-L., Montési, L.G.J. & Gaetani, G.A., 2014. Experimental quantification of permeability of partially molten mantle rock, *Earth planet. Sci. Lett.,* **388,** 273–282.

Park, H.-H. & Yoon, D.N., 1985. Effect of dihedral angle on the morphology of grains in a matrix phase, *Metall. Trans. A,* **16**(5), 923–928.

Price, J., Wark, D., Watson, E. & Smith, A., 2006. Grain-scale permeabilities of faceted polycrystalline aggregates, *Geofluids,* **6,** 302–318.

Renner, J., Viskupic, K., Hirth, G. & Evans, B., 2003. Melt extraction from partially molten peridotites, *Geochem. Geophys. Geosyst.,* **4**(5), 8606, doi:10.1029/2002GC000369.

Riley, G. & Kohlstedt, D., 1991. Kinetics of melt migration in upper mantle-type rocks, *Earth planet. Sci. Lett.,* **105,** 500–521.

Salters, V.J. & Longhi, J., 1999. Trace element partitioning during the initial stages of melting beneath mid-ocean ridges, *Earth planet. Sci. Lett.,* **166,** 15–30.

Smith, C.S., 1964. Some elementary principles of polycrystalline microstructure, *Metall. Rev.,* **9,** 1–48.

Spiegelman, M. & McKenzie, D., 1987. Simple 2-D models for melt extraction at mid-ocean ridges and island arcs, *Earth planet. Sci. Lett.,* **83,** 137–152.

Takei, Y., 2002. Effect of pore geometry on Vp/Vs: from equilibrium geometry to crack, *J. geophys. Res.,* **107,** ECV 6-1–ECV 6-12.

Team, T.M.S., 1998. Imaging the deep seismic structure beneath a Mid-Ocean Ridge: the MELT Experiment, *Science,* **280,** 1215–1218.

Vaughan, P. & Kohlstedt, D., 1982. Distribution of the glass phase in hot-pressed, olivine-basalt aggregates: an electron microscopy study, *Contrib. Mineral. Petrol.,* **81,** 253–261.

von Bargen, N. & Waff, H.S., 1986. Permeabilities, interfacial areas and curvatures of partially molten systems: results of numerical computations of equilibrium microstructures, *J. geophys. Res.,* **91,** 9261–9276.

Waff, H.S., 1974. Theoretical considerations of electrical conductivity in a partially molten mantle and implications for geothermometry, *J. geophys. Res.,* **79,** 4003–4010.

Waff, H.S. & Bulau, J.R., 1979. Equilibrium fluid distribution in an ultramafic partial melt under hydrostatic stress conditions, *J. geophys. Res.,* **84,** 6109–6114.

Wark, D.A. & Watson, E.B., 1998. Grain-scale permeabilities of texturally equilibrated, monomineralic rocks, *Earth planet. Sci. Lett.,* **164**, 591–605.

Wark, D.A. & Watson, E.B., 2000. Effect of grain size on the distribution and transport of deep-seated fluids and melts, *Geophys. Res. Lett.,* **27,** 2029–2032.

Wark, D.A., Williams, C.A., Watson, E.B. & Price, J.D., 2003. Reassessment of pore shapes in microstructurally equilibrated rocks, with implications for permeability of the upper mantle, *J. geophys. Res.,* **108,** 2050, doi:10.1029/2001JB001575.

Watson, H.C. & Roberts, J.J., 2011. Connectivity of core forming melts: experimental constraints from electrical conductivity and X-ray tomography, *Phys. Earth planet. Inter.,* **186,** 172–182.

Yoshino, T., Price, J.D., Wark, D.A. & Watson, E.B., 2006. Effect of faceting on pore geometry in texturally equilibrated rocks: implications for low permeability at low porosity, *Contrib. Mineral. Petrol.,* **152,** 169–186.

Yoshino, T., Laumonier, M., McIsaac, E. & Katsura, T., 2010. Electrical conductivity of basaltic and carbonatite melt-bearing peridotites at high pressures: implications for melt distribution and melt fraction in the upper mantle, *Earth planet. Sci. Lett.,* **295,** 593–602.

Zhu, W. & Hirth, G., 2003. A network model for permeability in partially molten rocks, *Earth planet. Sci. Lett.,* **212,** 407–416.

Zhu, W., Gaetani, G.A., Fusseis, F., Montesi, L.G.J. & De Carlo, F., 2011. Microtomography of partially molten rocks: three-dimensional melt distribution in mantle peridotite, *Science,* **332,** 88–91.